IOP Publishing and International Atomic Energy Agency Nuclear Fusion
Nucl. Fusion **49** (2009) 115026 (12pp) doi:10.1088/0029-5515/49/11/115026

Temporal behaviour of toroidal rotation velocity in the TCABR tokamak

J.H.F. Severo[1], I.C. Nascimento[1], Yu.K. Kuznetsov[1], R.M.O. Galvão[1,2], Z.O. Guimarães-Filho[1], F.O. Borges[1], O.C. Usuriaga[1], J.I. Elizondo[1], W.P. de Sá[1], E.K. Sanada[1] and M. Tendler[3]

[1] Institute of Physics, University of São Paulo, Rua do Matão, s/n, 05508-900 SP, Brazil
[2] Brazilian Center for Physics Research, Rua Xavier Sigaud 150, Rio de Janeiro BR-22290180, Brazil
[3] The Alfven Laboratory, EURATOM- Nuclear Fusion Research, Royal Institute of Technology 10044 Stockholm, Sweden

E-mail: jhsevero@if.usp.br

Received 27 March 2009, accepted for publication 16 September 2009
Published 21 October 2009
Online at stacks.iop.org/NF/49/115026

Abstract
A new method for determining the temporal evolution of plasma rotation is reported in this work. The method is based upon the detection of two different portions of the spectral profile of a plasma impurity line, using a monochromator with two photomultipliers installed at the exit slits. The plasma rotation velocity is determined by the ratio of the two detected signals. The measured toroidal rotation velocities of C III (4647.4 Å) and C VI (5290.6 Å), at different radial positions in TCABR discharges, show good agreement, within experimental uncertainty, with previous results (Severo *et al* 2003 *Nucl. Fusion* **43** 1047). In particular, they confirm that the plasma core rotates in the direction opposite to the plasma current, while near the plasma edge ($r/a > 0.9$) the rotation is in the same direction. This technique was also used to investigate the dependence of toroidal rotation on the poloidal position of gas puffing. The results show that there is no dependence for the plasma core, while for plasma edge ($r/a > 0.9$) some dependence is observed.

PACS numbers: 52.55.Fa

1. Introduction

Due to the relevance of plasma rotation for the stabilization of wall resistive modes, the achievement of improved confinement regimes, the transport of angular momentum and many other relevant physical mechanisms, the profiles of poloidal and toroidal rotation are being intensively investigated in many experiments. For reactor-size devices such as ITER, the external momentum input is expected to be small [1]. On the other hand, for wall resistive modes stabilization in ITER operational scenarios, some level of toroidal velocity is needed and it remains an open question whether the rotation generated by neutral beam injection will be enough to stabilize these modes. Therefore, it is very important to understand the physical mechanisms responsible for plasma rotation, in order to predict the plasma behaviour in reactor machines. In addition, there is no theoretical model that can reliably predict the toroidal plasma rotation in ITER and other large tokamaks; therefore, data from experiments are very important and can be used to develop useful empirical models.

It is well known that the poloidal velocity for a single plasma species is given by $U_{i\theta} = (k/M_i\omega_{ci})\partial T_i/\partial r$ where k is a coefficient that depends on the tokamak regime (equal to -1.83 for the collisional regime [2]), M_i is the ion mass, ω_{ci} is the ion cyclotron frequency and T_i is the ion temperature. A simple expression for impurity poloidal rotation velocity was obtained in [3]. For the case of TCABR, this expression gives $U_{i\theta} \simeq 10^3$–10^4 m s^{-1} and, indeed, careful measurements have shown that, in the collisional regime, the results agree reasonably well with the predictions of neoclassical transport theory [3, 4]. On the other hand, the toroidal velocity $U_{i\zeta}$ is of order 10^4–10^5 m s^{-1} and the experimental results are in disagreement with the neoclassical predictions [1, 5, 6].

As was pointed out above there is no theoretical model capable of reliably predicting the toroidal plasma rotation in axisymmetrically magnetically confined plasmas. Therefore, the plasma toroidal rotation is being investigated in several machines [7, 8]. In the TCV, by active charge exchange recombination spectroscopy, the radial profile of toroidal rotation has been carefully measured for a large range of plasma

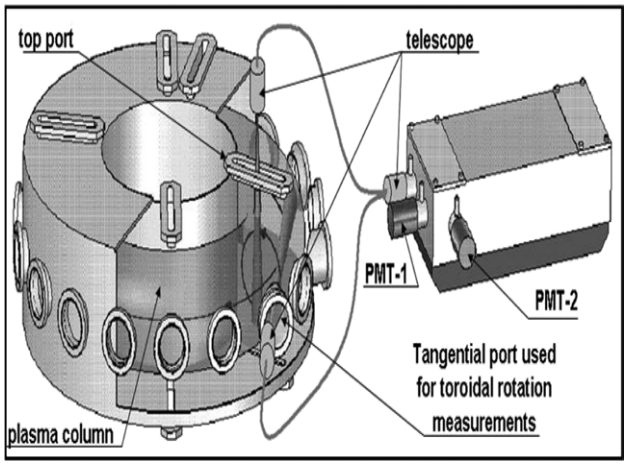

Figure 1. Experimental setup used for temporal evolution of plasma rotation velocity in the TCABR tokamak.

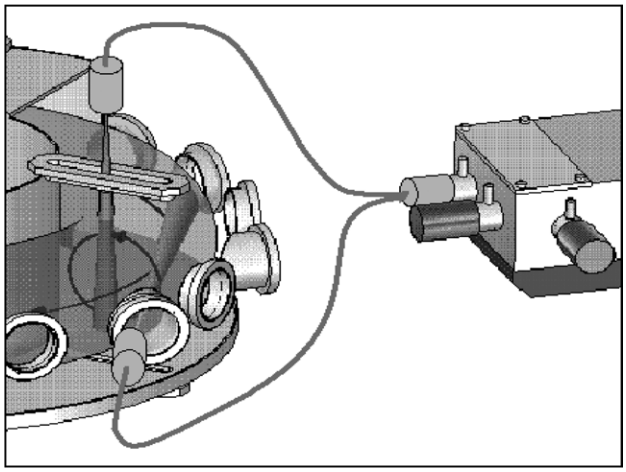

Figure 2. Detail of experimental setup.

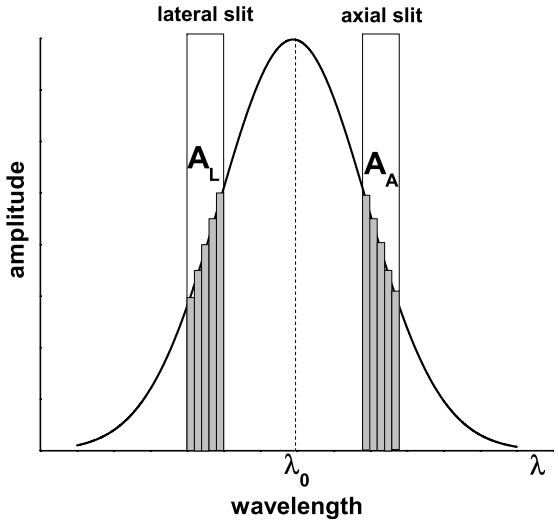

Figure 3. Schematic representation of the Gaussian spectral profile.

densities and edge safety factor [9]. It was observed that the maximum carbon velocity increases with the ion temperature and decreases with the plasma current.

Another important aspect of the toroidal rotation is its capability to rotate in both directions. In the TCV tokamak also, for ohmically heated plasmas, a spontaneous inversion from the counter-current to the co-current direction was observed. This inversion was described in [6] as related to a plasma density increase and it occurs in high current discharges. In the same machine [10], it was also observed that, in limiter configurations, the plasma core rotates in the counter-current direction and can reverse to the co-current one with a less than 10% increase in the plasma density. For diverted configurations, the plasma core rotates in the co-current direction reversing to the counter-current direction at high plasma density.

On MAST it was observed that the direction of the toroidal rotation changes from the co-current to the counter-current sense when switching from inboard to outboard gas puffing [11, 18]. In the TCABR tokamak, the plasma core rotates in the counter-current direction, while plasma edge rotates in the co-current direction, suggesting that the angular momentum for plasma edge is driven from the edge [3, 4].

One critical issue regarding the underlying mechanism associated with rotation is the poloidal and toroidal damping rate of rotation [12]. However, the charge exchange recombination spectroscopy diagnostic techniques used to measure temporal profiles do not have sufficient time resolution in particular for poloidal damping measurements where the time scale is of the order of the ion–ion collision time and, in general, this diagnostic is not available in small laboratories. This diagnostic can also introduce momentum into the plasma from the power beam. Other methods, such as Mach probes, can be used, but only for edge measurements.

A new method for measuring the temporal evolution of plasma rotation in tokamaks is reported in this work. The method is based on the ratio of the signals corresponding to the detection of two portions of the same impurity emission line, using two photomultipliers installed at the exit slits of a monochromator (figures 1 and 2). The light from the plasma is collected and transmitted to the entrance slit of the monochromator through an optical fibre. Inside the monochromator, using a semi-transparent mirror, the light is divided into two parts and directed to the photomultipliers located at the exit slits. The lateral exit slit 2 integrates the left part (area A_L in figure 3) of the spectral line profile and the axial slit 1 integrates its right part. Therefore, as the plasma moves, the centre of the spectral line will move to the right or left, changing the ratio $R = A_L/A_A = R(\Delta\lambda_0)$, which is proportional to the plasma rotation velocity. Here $\Delta\lambda_0$ is the Doppler shift of the spectral line.

The rest of the paper is organized as follows. The apparatus and methodology are described in section 2. In section 3, a general expression for plasma rotation as a function of signal ratio is derived and the possible influence of the ion temperature on signal ratio is evaluated. The technique used to obtain a relative calibration is described in section 4. Section 5 is dedicated to show illustrative results of the neoclassical theory and its application to investigate the dependence of toroidal rotation on the poloidal position of gas puffing. The experimental results are presented in section 6. Discussions and conclusions are given in section 7. Appendix A is dedicated to the error analysis and appendix B to the evolution of the radial profile of toroidal rotation.

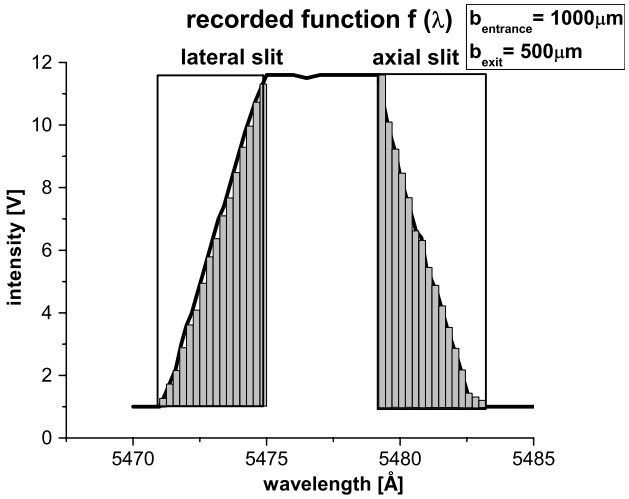

Figure 4. Experimental contour used for plasma rotation measurements in the TCABR tokamak.

2. Apparatus and methodology

The temporal evolution of toroidal rotation velocity in the TCABR tokamak was measured using a $f/8.4$ Czerny-Turner optical monochromator (Jobin-Yvon, THR 1000), employing commercial grating with a 1200 g mm^{-1} and two R93-2 (Hamamatsu) photomultipliers installed at the exit slits. The monochromator has the focal length of 1000 mm and inverse dispersion of 8 Å mm^{-1}. The monochromator is equipped with a stepping motor with 0.01 Å per step and the grating scan rate is about 70 Å s^{-1}.

The optical measurement system is shown in figures 1 and 2. The light from the plasma is collimated with a telescope ($f = 50$ mm) and transmitted to the entrance slit of the monochromator through an optical fibre of 1 mm diameter. In front of the entrance slit there are two lenses with apertures $f/4$ and $f/8$ to collimate the light beam from optical fibres transmitted to the monochromator. To register the signals of the photomultipliers, a two channel oscilloscope with sampling rate of 1 GS s^{-1} and 60 MHz of bandwidth was used. The Doppler shift is calculated from the ratio of the signals of the photomultipliers, as described in the following.

The signal ratio does not depend on detector or circuit parameters. Indeed, the possible differences related to detector sensitivity, amplifier gain, etc can be removed by relative calibration and therefore the signal ratio depends just on the Doppler shift.

To obtain a linear dependence of signal ratio on the Doppler shift of the emission line, its Gaussian shape was changed to a trapezoidal one through an increase in the width of the entrance slit. Figure 4 shows a new trapezoidal shape of line obtained with 1000 μm and 500 μm widths of the entrance and exit slits, respectively.

With this procedure, the shape of the recorded signal $f(\lambda)$, which is a convolution of two functions, $g(\lambda)$ (spectral profile of spectral line) and $a(\lambda)$ (apparatus function), has a trapezoidal form if the full-width at half-maximum (FWHM) of $g(\lambda)$ is much smaller than $a(\lambda)$. As can be seen from figure 4, the convolution of these two lines gives a trapezoidal shape and working with this new shape is more convenient because a possible change in the spectral profile of the spectral impurity line cannot affect the signal ratio, increasing the sensibility of the diagnostic.

One important aspect of this technique is that the direction of plasma rotation can be rather easily determined; the signal ratio $R = A_L/A_A$ is below unit when the Doppler shift is in the red direction (figure 3) and above unit when the shift is in the blue direction.

3. Plasma velocity as a function of signal ratio

From figure 3 we can see that the dependence of the signal ratio on the Doppler shift is directly connected with the shape of the recorded contour $f(\lambda)$. On the other hand, it is well known that the recorded contour $f(\lambda)$, which is the intensity distribution of the spectral line, broadened by two effects, is expressed by the equation

$$f(\lambda) = \int_{-\infty}^{+\infty} g(\lambda')a(\lambda - \lambda')\,\mathrm{d}\lambda', \tag{1}$$

where $g(\lambda)$ is contour of the spectral line that has, in most cases, a Gaussian profile, and $a(\lambda)$ is the apparatus function.

A general method to solve equation (1) consists of representing the functions $g(\lambda)$ and $a(\lambda)$ in the form of a Fourier integral

$$g(\lambda) = \frac{1}{\sqrt{2\pi}} \int_{-\infty}^{+\infty} G(\omega)\mathrm{e}^{\mathrm{i}\omega\lambda}\,\mathrm{d}\omega$$

$$a(\lambda) = \frac{1}{\sqrt{2\pi}} \int_{-\infty}^{+\infty} A(\omega)\mathrm{e}^{\mathrm{i}\omega\lambda}\mathrm{d}\omega. \tag{2}$$

Then equation (1) can be rewritten as

$$f(\lambda) = \frac{1}{2\pi} \int_{-\infty}^{+\infty} G(\omega)A(\omega)\mathrm{e}^{\mathrm{i}\omega\lambda}\,\mathrm{d}\omega, \tag{3}$$

where

$$A(\omega) = \frac{1}{\sqrt{2\pi}} \int_{-\infty}^{+\infty} a(\lambda)\mathrm{e}^{-\mathrm{i}\omega\lambda}\,\mathrm{d}\lambda \tag{4}$$

is the Fourier transform of the apparatus function.

Equation (3) can be rewritten in the following way:

$$f(\lambda) = \frac{1}{2\pi} \int_{-\infty}^{+\infty} [G(\omega) - 1 + 1]A(\omega)\mathrm{e}^{\mathrm{i}\omega\lambda}\,\mathrm{d}\omega,$$

that is,

$$f(\lambda) = \frac{1}{2\pi} \int_{-\infty}^{+\infty} [G(\omega) - 1]A(\omega)\mathrm{e}^{\mathrm{i}\omega\lambda}\,\mathrm{d}\omega + a(\lambda). \tag{5}$$

The first term in equation (5), called the correction term, is very small in our case ($\mathrm{FWHM}_{\mathrm{monochr}} \gg \mathrm{FWHM}_{\mathrm{impurity}}$). Actually, it vanishes in the ideal case of monochromatic illumination, so that the recorded contour $f(\lambda)$ will be equal to the apparatus function. The correction term gives a small effect connected with the dependence of the Gaussian profile on the temperature of the impurity ion.

To find the signal ratio dependence on the Doppler shift, we assume that the apparatus function can be expressed in the

following form [13]

$$a(\lambda)=\begin{cases}\dfrac{1}{S_1}; & S_1>S_2;\ |\lambda|\leqslant\dfrac{S_1-S_2}{2}\\ \dfrac{1}{S_1S_2}\left(\dfrac{S_1+S_2}{2}-|\lambda|\right); & \dfrac{S_1-S_2}{2}\leqslant|\lambda|\leqslant\dfrac{S_1+S_2}{2}\\ 0; & \dfrac{S_1+S_2}{2}\leqslant|\lambda|\end{cases}. \tag{6}$$

Here $S_2=b_{A,L}d_\lambda$ is the width of the geometric image of the exit slit and $S_1=b_E d_\lambda$ is the width of the geometric image of the entrance slit, $b_{A,L}$ is the exit width of the lateral or axial slit, b_E is the width of the entrance slit, d_λ is the inverse dispersion and λ is the wavelength of the impurity line.

Expanding the Fourier transform of the Gaussian function in a Taylor series and substituting in (5) yields

$$f(\lambda)=-\frac{1}{2\pi}\int_{-\infty}^{+\infty}\sigma^2\omega^2A(\omega)e^{i\omega\lambda}d\omega+a(\lambda),$$

where σ is, in the case of the Gaussian function, proportional to the square root of the ion temperature T_i.

Taking into account (2), we can write

$$\frac{d^2a(\lambda)}{d\lambda^2}=-\frac{1}{2\pi}\int_{-\infty}^{+\infty}\omega^2A(\omega)e^{i\omega\lambda}d\omega.$$

Therefore we have

$$f(\lambda)=a(\lambda)+\sigma^2\frac{d^2a(\lambda)}{d\lambda^2}. \tag{7}$$

Equation (7) gives the recorded contour $f(\lambda)$ as a function of the apparatus function and its derivative. The second term in the right-hand side is the correction term that is proportional to the ion temperature.

To obtain a strong dependence of the signal ratio on the Doppler shift, the photomultipliers could integrate the recorded function where there is strong variations of its shape with wavelength, which means to integrate the function $f(\lambda)$ in the following two intervals: $\lambda_L-\Delta\lambda_L/2$ to $\lambda_L+\Delta\lambda_L/2$ and $\lambda_A-\Delta\lambda_A/2$ to $\lambda_A+\Delta\lambda_A/2$, where λ_L and λ_A are the points on the left and right part of apparatus function where its height is one half of the maximum for no Doppler shifted line; $\Delta\lambda_L=b_Ld_\lambda$ and $\Delta\lambda_A=b_Ad_\lambda$ are limits of integration that are determined just by width of axial and lateral slits (see figure 5).

Since we are analysing the ideal case where apparatus function is described by (6), the second term on the right side of (7) is equal to zero, so we can write

$$A_L=\int_{\lambda_L+\Delta\lambda_0-\frac{\Delta\lambda_L}{2}}^{\lambda_L+\Delta\lambda_0+\frac{\Delta\lambda_L}{2}}f(\lambda)d\lambda=\int_{\lambda_L+\Delta\lambda_0-\frac{\Delta\lambda_L}{2}}^{\lambda_L+\Delta\lambda_0+\frac{\Delta\lambda_L}{2}}a(\lambda)d\lambda,$$

and

$$A_A=\int_{\lambda_A+\Delta\lambda_0-\frac{\Delta\lambda_A}{2}}^{\lambda_A+\Delta\lambda_0+\frac{\Delta\lambda_A}{2}}f(\lambda)d\lambda=\int_{\lambda_A+\Delta\lambda_0-\frac{\Delta\lambda_A}{2}}^{\lambda_A+\Delta\lambda_0+\frac{\Delta\lambda_A}{2}}a(\lambda)d\lambda.$$

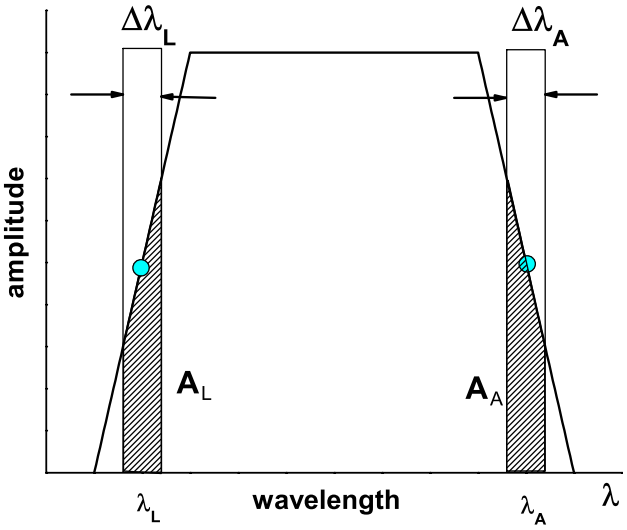

Figure 5. Schematic representation of trapezoidal contour.

The above equation gives the areas A_L and A_A as a function of the Doppler shift $\Delta\lambda_0$. To find the signal ratio dependence on the Doppler shift, we take the ratio between A_L and A_A so that

$$A_L=\frac{\Delta\lambda_L}{2S_1S_{2L}}(S_{2L}+2\cdot\Delta\lambda_0) \qquad \text{and}$$

$$A_A=\frac{\Delta\lambda_A}{2S_1S_{2A}}(S_{2A}-2\cdot\Delta\lambda_0).$$

Then, the ratio between A_L and A_A is equal to

$$R=\frac{(S_{2L}+2\cdot\Delta\lambda_0)}{(S_{2A}-2\cdot\Delta\lambda_0)}\Rightarrow\Delta\lambda_0=\frac{1}{2}\left(\frac{RS_{2A}-S_{2L}}{R+1}\right). \tag{8}$$

Here S_{2L} and S_{2A} are the width of the geometric image of the lateral and axial exit slits which are equal to the integration limits $\Delta\lambda_L$ and $\Delta\lambda_A$, respectively.

Equation (8) gives a simple expression for the Doppler shift as a function of the signal ratio R and geometrical parameters. However, its derivation is based upon many simplified assumptions that are not completely justified as discussed in the next paragraph. Despite this, it will be shown that it is useful for small rotation velocities and for error analysis.

To obtain the dependence of the signal ratio on the Doppler shift with adequate accuracy, we need to take into account many distorting factors such as diffraction, aberration of the optical system, finite aperture widths, stray light and light scattering on the slits, which distort the recorded function $f(\lambda)$ and are difficult to quantify. A way out of this difficulty is to obtain the actual apparatus function using as a light source a simple lamp with a spectral line near the spectral line of the plasma impurity. The influence of a Gaussian profile on the real apparatus function can then be calculated using a numerical scheme for the convolution of two functions.

Figure 6 shows the dependence of the signal ratio on the Doppler shift obtained with equation (8) and by a convolution of the apparatus and Gaussian functions, for ion temperature $T_i=150$ eV. It can be seen that, although the analytical

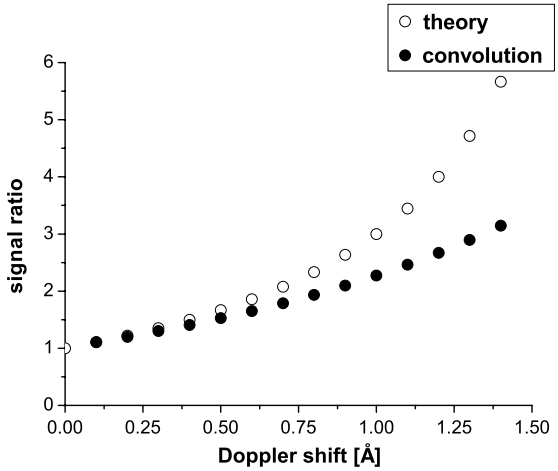

Figure 6. Dependence of signal ratio on the Doppler shift obtained theoretically (empty circle) and by a computation (full circle) of convolution of $g(\lambda)$ (spectral profile of spectral line) and $a(\lambda)$ (apparatus function) for ion temperature of 150 eV.

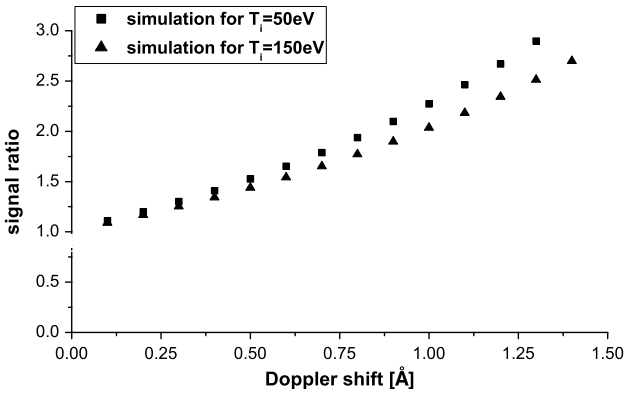

Figure 7. Simulation of the dependence of signal ratio on the Doppler shift for two different ion temperatures (50 and 150 eV).

expression always gives a larger signal ratio, it can be reliably used for Doppler shifts below 0.5 Å, corresponding to a rotation velocity $V = 30\,\mathrm{km\,s^{-1}}$. However, this result depends on the ion temperature. Indeed, as can be inferred from figure 3, if the ion temperature increases the shape of the recorded function changes, its variation can influence the dependence of signal ratio on the Doppler shift. To better investigate this effect, we computed the convolution of the apparatus function with the Gaussian function where the FWHM of this function corresponds to the ion temperature equal to 50 and 150 eV and takes the ratio of the integrals of left and right sides as a function of the Doppler shift. The results for these two different temperatures are shown in figure 7; it can be seen that the influence of the ion temperature is small and can be easily ignored for the TCABR parameters.

For machines where ion temperature is high (larger than 1 keV), we can always chose some combination of entrance and exist slit widths such that the recorded function $f(\lambda)$ has a trapezoidal shape and possible variations of the ion temperature will not have an influence on signal ratio. Another way to avoid this effect is to work with heavy impurities. Therefore, the method described here can usually be adapted to be weakly sensitive to the effect of changes in the ion temperature.

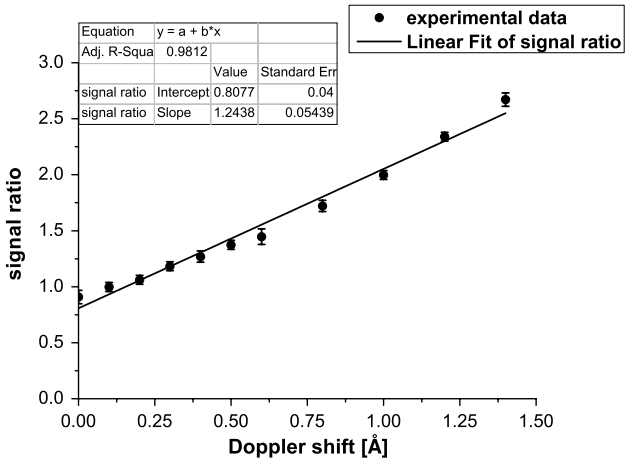

Figure 8. Experimental dependence of signal ratio on the Doppler shift for the C VI (5290.6 Å) carbon spectral line obtained with the collimating system (telescope) placed at the position of the magnetic axis where poloidal rotation is approximately equal to zero.

4. Calibration

The intensity of the primary signal depends on various parameters that can be classified in four different groups. The first group includes plasma parameters such as plasma density, electron temperature and ion density. The second group includes spectral line parameters as the coefficient rate for a specific transition. The third group includes all parameters related to the measuring equipment as monochromator, slit width, detector characteristics, as quantum efficiency, circuit characteristics, as amplifier gain, voltage divider circuit for the case of a photomultiplier tube detector (PMT). Finally, the fourth group includes the Doppler shift of the spectral line that is to be measured. The parameters included in the first and second groups cancel each other when the ratio of the signals of the photomultipliers is taken. The parameters of the third group can be easily relatively calibrated. The parameters of the fourth group depend only on plasma velocity, which is determined by signal ratio.

The relative calibration of the parameters of the third group was done in the following way. A spectral line of a calibration lamp was scanned, by rotation of the diffraction grating of the monochromator, and the spectral distributions obtained in both detectors are recorded. The amplitude of the signals were adjusted by increasing or reducing the amplifier gain, power voltage in the divider circuit, or slit width, to obtain a signal ratio approximately equal to unit.

To properly calibrate the parameters of the fourth group, the line of sight of the detection system was placed at the position of the magnetic axis and the signals adjusted to yield the expected zero poloidal rotation. Then the carbon lines C III (4647.4 Å) and C VI (5290.6 Å) were scanned, in a shot-to-shot bases, and the dependence of the signal ratio on the Doppler shift was obtained for these lines (figure 8). The plasma rotation velocity was then calculated.

A simple error analyses based upon equation (8) is presented in appendix A. There it is shown that, for the conditions of experiments carried out in TCABR, the standard deviation in the measurements of the Doppler shift, $\sigma_{\Delta\lambda_0}$, is approximately one fourth of the standard deviation in the

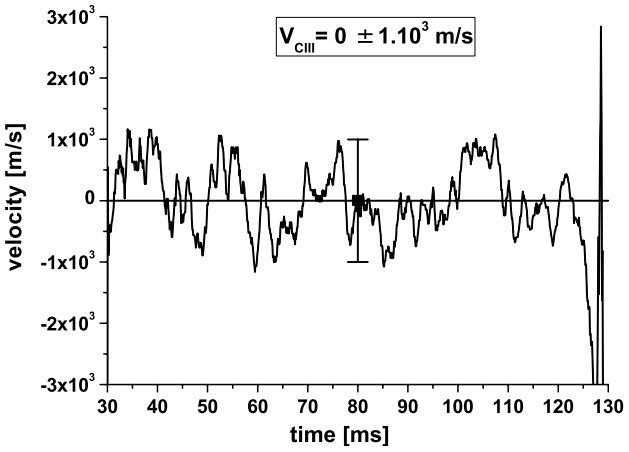

Figure 9. The poloidal rotation velocity measurements of C III (4647.4 Å) in the plasma centre where the expected value is zero. The error bars indicate the uncertainty obtained by propagation (equation (A1)).

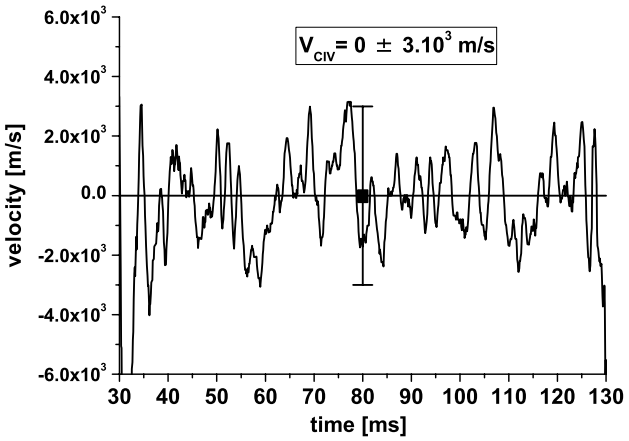

Figure 10. The poloidal rotation velocity measurements of C VI (5290.5 Å) in the plasma centre where the expected value is zero. The error bars indicate the uncertainty obtained by propagation (equation (A1)).

determination of the signal ratio (σ_R) multiplied by the width of the geometric image of the exit slits (S_2) (see figures 9 and 10).

5. Relevant theoretical results on plasma rotation

The poloidal velocity component V_i^θ can be found from the magnetic surface average of the parallel component of the momentum equation

$$\left\langle \boldsymbol{B}\cdot M_i n \frac{\mathrm{d}_i \boldsymbol{V}_i}{\mathrm{d}t}\right\rangle = -\langle \boldsymbol{B}\cdot\boldsymbol{\nabla} p\rangle - \langle \boldsymbol{B}\cdot\boldsymbol{\nabla}\cdot\pi\rangle + \frac{1}{c}\langle \boldsymbol{B}\cdot[\boldsymbol{j}\times\boldsymbol{B}]\rangle. \tag{9}$$

For a steady-state case we obtain

$$\langle \boldsymbol{B}\cdot\boldsymbol{\nabla}\cdot\pi\rangle = \int_0^{2\pi} \mathrm{d}\theta \left(M_i \tilde{n} \frac{\boldsymbol{B}}{B^\theta}\cdot\frac{\mathrm{d}_i \boldsymbol{V}_i}{\mathrm{d}t} - \frac{3}{2}\pi_\parallel \frac{\partial \ln B}{\partial\theta}\right) = 0. \tag{10}$$

Solving equation (10), we obtain the classical expression for poloidal rotation [14, 15] which demonstrates the primary role of the ion viscosity in inducing residual plasma flows and radial electric fields in fully ionized plasmas. The main result of this theory is that $U_{i\theta}$ is proportional to the gradient of the ion temperature,

$$U_{i\theta} = kU_{T_i}, \qquad U_{T_i} = \frac{1}{M_i\omega_{ci}}\frac{\partial T_i}{\partial r}, \tag{11}$$

where the coefficient k depends on the tokamak regime.

From equation (10) it follows that the only mechanism responsible for poloidal rotation is parallel viscosity. The reason for this is the term proportional to $\partial T_i/\partial r$, which is called thermal force, and acts as a drive for rotation.

However, there might exist more than one driving mechanism responsible for toroidal rotation without momentum input. The neoclassical torque has been determined in [16] for the collisional regime. In [17] it was demonstrated that, in the absence of external momentum sources, the transport of angular momentum is sensitive to the poloidal location of gas injection, the toroidal rotation velocity is proportional to the ion temperature gradient and the plasma rotates in the counter-current direction. The authors of this work have obtained a simple expression for the toroidal rotation velocity that can be verified in a simple tokamak experiment, such as the one carried out in TCABR.

6. Experimental results

For small aspect ratio, $\epsilon \ll 1$ and circular cross section, the toroidal velocity can be expressed as [17]

$$V_{i\varphi} \simeq \frac{2\epsilon}{eB_\theta}\frac{\mathrm{d}T_i}{\mathrm{d}r}[k\cos\theta - (k-1)\cos\theta_*], \tag{12}$$

where $k = 5/2 - 0.7/Z_{\mathrm{eff}}$; θ is the poloidal angle and θ_* is the poloidal angle of gas puffing.

To verify the dependence of toroidal rotation on the poloidal location of neutral gas injection, three stainless-steel injection tubes (3.4 mm internal diameter) were installed on the vacuum chamber of TCABR, at the poloidal position $\theta_* = 0$ (outboard), $\theta_* = \pi/2$ (top) and $\theta_* = \pi$ (inboard), (see figure 11). The toroidal rotation velocity was then measured at different radial positions. For positions with approximately the same ion temperature gradient, the above expression predicts a change in the value of the rotation velocity by a factor around $(2k-1)$, from inboard to outboard injection, which should be easily detected. However, since TCABR has a full poloidal graphite limiter, recycling from it may somewhat partially smooth out the effect of localized gas injection.

The major parameters of TCABR are the following: minor radius $a = 0.18$ m, major radius $R = 0.61$ m and toroidal magnetic field $B_T = 1.1$ T. For this experimental campaign, the discharge parameters were the following: plasma current $I_P = 100$ kA, average density $n_e \simeq (1\text{–}4.5) \times 10^{13}$ cm^{-3}, $T_e(0) \simeq 600$ eV, $T_i(0) \simeq 200$ eV, and the plasma was mainly in the collisional Pfirsch–Schluter regime. The duration of the stationary phase of the discharge was 60 ms. Because of the graphite limiter, the main impurity in the hydrogen discharges was carbon; therefore, the carbon lines C III (4647.4 Å) and C VI (5290.6 Å) appear as natural choices for rotation measurements.

The temporal behaviour of the line-integrated toroidal rotation velocity is shown in figures 12 and 13 at radial

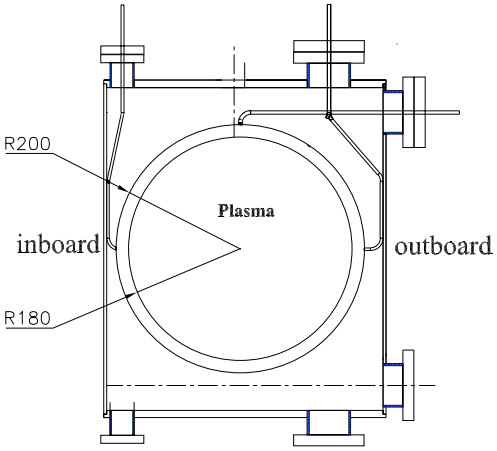

Figure 11. Scheme of the poloidal position of gas puffing used in the TCABR experiments ($\theta_* = 0$, outboard; $\theta_* = \pi/2$, top and $\theta_* = \pi$, inboard).

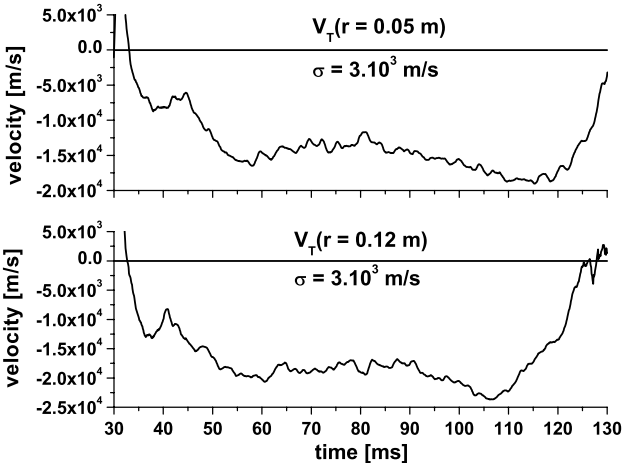

Figure 12. Temporal evolution of the toroidal rotation velocity of C VI (5290.6 Å) at $r = 0.05$, and 0.12 m radial positions. The negative value of the velocity means that the impurity rotates in the counter-current direction.

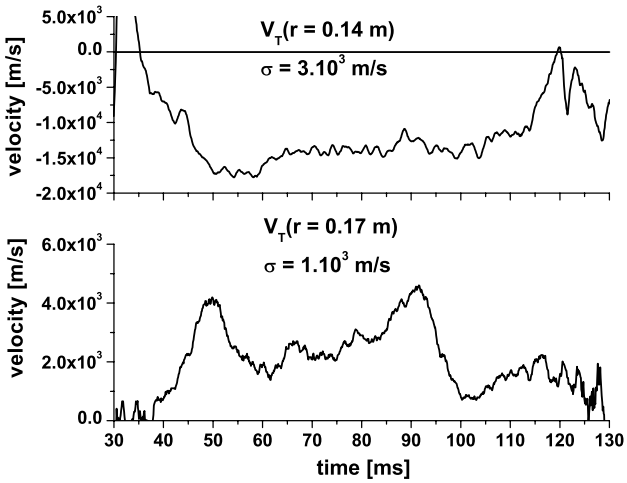

Figure 13. Temporal evolution of the toroidal rotation velocity of C VI (5290.6 Å) and C III (4647.4 Å) at 0.14 and 0.17 m radial positions. The positive value of the velocity at the 0.17 m radial position means that the impurity rotates in the co-current direction.

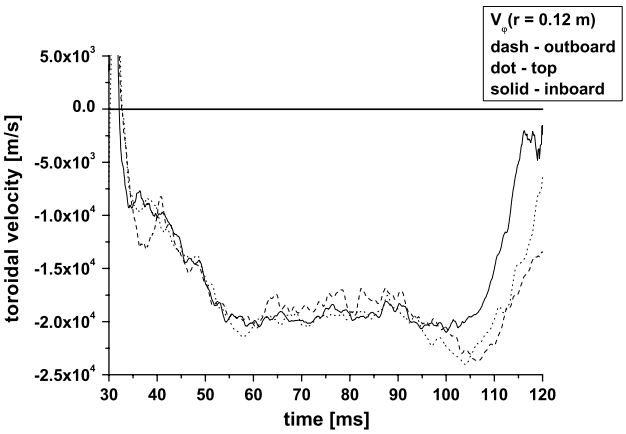

Figure 14. Temporal evolution of the toroidal rotation velocity of C VI (5290.6 Å) at the $r = 0.12$ m radial position for $\theta_* = 0$, outboard (dash); $\theta_* = \pi/2$, top (dot) and $\theta_* = \pi$, inboard (solid).

positions $r = 0.05$, 0.12, 0.14 and 0.17 m for different shots. At radial position $r = 0.16$ and $r = 0.17$ m, the rotation velocity was evaluated with C III (4647.4 Å) carbon line and its experimental uncertainty (appendix A) is approximately 1×10^3 m s^{-1}. At radial positions $r = 0.05$, 0.10, 0.12 and 0.14 m, the rotation velocity was measured with C VI (5290.6 Å) and the experimental uncertainty is approximately 3×10^3 m s^{-1}.

These results show that the direction of the toroidal velocity of the plasma core is opposite to the direction of the plasma current and it changes sign at the plasma edge i.e. $r \geqslant 0.16$ m.

The dependence of the toroidal rotation velocity on poloidal injection of the hydrogen gas was also measured for different radial positions ($r = 0.05$, 0.10, 0.12, 0.14, 0.16 and 0.17 m). Figure 14 shows the line-integrated temporal evolution of the toroidal rotation velocity at $r = 0.12$ m for three different poloidal positions ($\theta_* = 0$, outboard; $\theta_* = \pi/2$, top and $\theta_* = \pi$, inboard) of gas injection. Figure 15 shows the ratio of inboard to outboard rotation velocity for different radial positions. The ratio was obtained taking into account the mean velocity in the interval between 60 and 90 ms. As can be inferred from this figure, the poloidal position of gas puff does not have a strong effect on the rotation velocity that is predicted by theory [17]. However, a small effect is observed at the plasma edge where outboard injection produces larger rotation velocity than inboard injection. This effect suggests some analogy with the effect that was observed on MAST [18], where the direction of the toroidal rotation velocity inside the separatrix depends on the position (inboard, outboard) of gas puff and where inboard injection produces counter-rotation while outboard produces co-rotation.

The small influence of gas puff on rotation velocity is consistent with the simple evolution of the magnitude of inward gas puff, Φ_{Pin}, required to maintain the plasma density constant during the stationary phase of the discharge. Representing the sufarce-averaged inward flux coming from recycling at the walls and limiter by Φ_{Rin}, the condition for constant

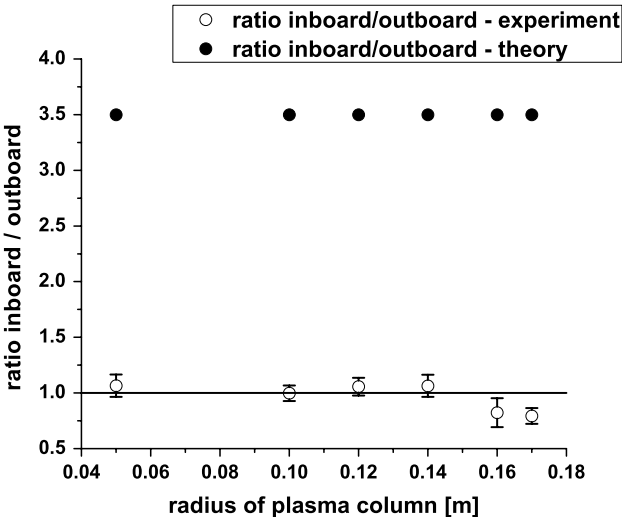

Figure 15. Ratio of inboard to outboard of the toroidal rotation velocity for different radial positions in the TCABR experiment. The full circles represent the same ratio calculated from the model that is proposed in [17].

density is

$$\Phi_{\mathrm{Pin}} + \Phi_{\mathrm{Rin}} = \Phi_{\mathrm{out}} = \frac{\langle n_{\mathrm{e0}} \rangle}{\tau_{\mathrm{p}}} V_{\mathrm{P}}, \tag{13}$$

where Φ_{out} is the outward flux of the particle that crosses the last magnetic surface, τ_{p} is the particle confinement time, $\langle n_{\mathrm{e0}} \rangle$ is the central line averaged plasma density and V_{P} is the plasma volume. Taking $\tau_{\mathrm{p}} \simeq 10$ ms (as evaluated from density decay estimates [19]) and $\langle n_{\mathrm{e0}} \rangle \simeq 1.5 \times 10^{19}\,\mathrm{m}^{-3}$, we have $\Phi_{\mathrm{out}} \simeq 6 \times 10^{18}$ particles s^{-1}, while the inward gas puff flux is $\Phi_{\mathrm{Pin}} \simeq 5 \times 10^{17}$ particles s^{-1}. Therefore $\Phi_{\mathrm{out}} \gg \Phi_{\mathrm{Pin}}$, so that the plasma rotation at the edge is determined mainly by the recycling, e.g., by the inward flux coming from the scrape-off layer that is poloidally symmetric.

It is important to understand that the underlying physics of rotation in the tokamak is the radial profile of the rotation velocity. Unfortunately, the simple spectroscopy technique gives only line-integrated signals. With a sufficient number of lines of sight, it is possible, in principle, to obtain the radial profiles by Abel inversion [20, 21]. In our case there is only a small number of lines of sight making Abel inversion unreliable. Despite this, since the radial profile of the toroidal rotation velocity is expected to have a well-behaved radial dependence, we can estimate it by assuming a simple polynomial dependence, $V(r) = c_0 + c_1 r + c_2 r^2 + c_3 r^3$ where c_0, c_1, c_2 and c_3 are some constants to be determined. Calculating the ratio R of the signals measured at the lateral and axial slits of the monochromator, we can obtain the expression for the unknown coefficients and determine the toroidal rotation profile. This procedure is described in appendix B.

The radial profile of the emissivity of the C III (4647.4 Å) and C VI (5290.6 Å) spectral lines is shown in figure 16. The radial profile of the toroidal rotation velocity is also shown in figure 17 for $\theta_* = 0$, together with the direct measurements made along six lines of sight. It is readily seen that, in spite of the roughness of this procedure, the obtained radial profile is rather reasonable and gives a good fitting for further numerical modelling of the discharge.

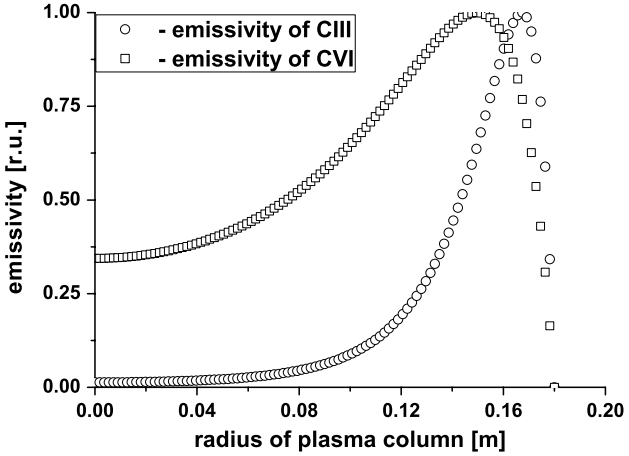

Figure 16. The radial profile of the emissivity of the C III (4647.4 Å) and C VI (5290.6 Å) spectral lines.

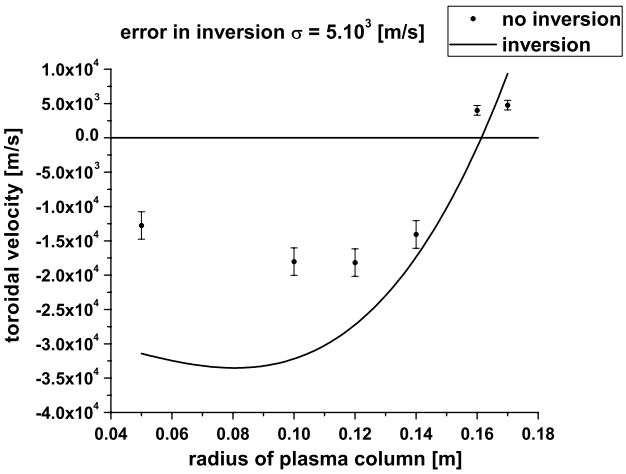

Figure 17. The radial profile of the toroidal rotation velocity in the TCABR tokamak. The experimental uncertainty in the line-integrated measurements is $3 \times 10^3\,\mathrm{m\,s}^{-1}$ while in the profile results it is $5 \times 10^3\,\mathrm{m\,s}^{-1}$.

Comparing the results of rotation velocity before and after the inversion procedure in figure 17, we can observe, as expected, that the line-integrated measurements are closer to inverted only for the plasma edge where the closest point coincides with the position of maximum emissivity of the C VI carbon line. In the central region, the difference between them is more prominent which suggests that the velocity inversion is a necessary and important process for receiving correct information about the velocity profile.

As was pointed out in the introduction, in the TCV machine it was observed that the maximum carbon velocity increases with the ion temperature [9] suggesting $v(r) \propto T_{\mathrm{i}}(r)$. Supposing we have $T_{\mathrm{i}}(r) \simeq T_0[1-(r/a)^2]^{\alpha}$ it yields $v(r) \simeq T_0[1 - 2\alpha r^2/\ a^2 + 2(\alpha - 1) r^4/a^4]$. For the TCABR $\alpha \simeq 1$ which implies that the velocity profile has parabolic behaviour. In [17] the authors have theoretically obtained an expression for the toroidal rotation velocity where it is proportional to the ion temperature gradient, e.g. $v(r) \propto \partial T_{\mathrm{i}}(r)/\partial r$. For the TCABR case it implies $v(r) \propto r$ which is less realistic as can be observed in figure 17.

7. Discussions and conclusions

A new diagnostic method for determining the temporal evolution of plasma rotation in tokamaks was developed based upon the detection of different portions of the same spectral profile of a plasma impurity line and applied to determine the toroidal rotation profile in TCABR discharges. One of the relevant characteristics of this method is that the results are not strongly affected by possible fluctuation in the ion temperature during a measurement. A simple expression for the Doppler shift was derived, neglecting corrections to the impurity line profile due to experimental distortion factors, which applies for rotation velocities below 30 km s^{-1}, for the conditions of TCABR discharges. For rotation velocities larger than this value, an experimental calibration procedure was employed, giving an uncertainty in the measurements around 1–3 km s^{-1}.

The measured toroidal rotation velocities vary from -20 km s^{-1} (at $r = 0.12$ m) to +3 km s^{-1} (at $r = 0.17$ m). Here negative values refer to counter plasma current. These values agree reasonably well, within experimental uncertainty, with previous results [3, 4] and with the results obtained in other small tokamak experiments [22, 23].

The toroidal rotation inversion is possibly related to the outward flux of ions, which is larger at the plasma edge, producing a torque in the co-current direction ($q\boldsymbol{V}_r \times \boldsymbol{B}_\theta$). Furthermore, impurity ions may escape at the plasma edge with a large electric charge. They recombine in the scrape-off layer and the ions of the compensating influx usually have a small charge, being further ionized as they penetrate towards the centre of the plasma. This unbalanced ion charge flux may drive a toroidal torque in the co-current direction.

The results of the experiment carried out to verify the dependence of the toroidal rotation velocity on the poloidal location of neutral gas injection indicate that there is no influence in the central region of the plasma; a small effect was observed only at the plasma edge.

Comparing the diagnostic technique that was used for toroidal rotation measurements in the TCABR tokamak with the charge exchange recombination spectroscopy diagnostic technique, we can point out some positive and negative aspects in both of them. For example, the charge exchange recombination spectroscopy is widely used to measure the impurity density, ion temperature and rotation velocity profile with high spatial (∼0.3cm) [24] and temporal resolution (<1 ms) [25]. However, it was well pointed out by Solomon *et al* [26] that, while the basic principle of determining the velocity from the Doppler shift of a spectral line is relatively simple, the interpretation of this shift is complicated by atomic physics effects. Although our diagnostic system was build to measure just one spatial point and has temporal resolution of 1 ms, this diagnostic can be very easily updated to measure rotation velocities with good spatial resolution and time resolution better than 1 μs; furthermore, the rotation velocity is obtained readily in real time. Two other important aspects of the charge exchange recombination spectroscopy technique are cost and that the rotation velocity can be directly inferred without an inverse process. Our technique provides only line-integrated measurements and has a relatively small cost.

A similar technique was employed by Paul *et al* [27] for rotation measurements. In this work the plasma rotation was inferred by employing two detectors and interference filters that have positive and negative pass band slope and observe the same plasma volume. The Doppler shift is obtained from the ratio of signals coming from both detectors. In this diagnostic a bundle of seven 1 mm diameter optical fibres was also used to transmit the light from the tokamak to the detectors, which implies a viewing area of approximately 18 cm^2. To avoid that the individual fibre observe regions of different emissions, the light was homogenized by inserting a mode mixer silica rod.

Even though this technique is similar to that used in the TCABR tokamak experiment, some differences (positive and negative aspects) can be pointed out. Firstly, the dependence of signal ratio on the Doppler shift and its linearity depend strongly on the filter characteristics and the ability of the manufacturer to construct this filter with the required specifications for each kind of experiment. In our case, the dependence of signal ratio on the Doppler shift can be chosen by an adequate choice of the entrance and exit slits widths of the monochromator. Secondly, these filters can be used to measure the Doppler shift of just one spectral line, while using monochromator you can in shot-to-shot bases measure the Doppler shift of a wide range of different spectral lines. Finally, the cost of these two diagnostics is quite different.

Acknowledgments

This work was partially supported by the Foundation for Supporting Research of the State of São Paulo (FAPESP), the the National Fusion Network (RNF/FINEP) and the National Councel of Research and Technological Development (CNPq).

Appendix A. Error analysis and time resolution

The uncertainty in measuring rotation velocity can be obtained from the derivative of equation (8),

$$\begin{aligned}\sigma^2_{\Delta\lambda_0} &= \left(\frac{\partial\Delta\lambda_0}{\partial R}\right)^2\sigma^2_{\mathrm{R}} + \left(\frac{\partial\Delta\lambda_0}{\partial S_{2\mathrm{L}}}\right)^2\sigma^2_{S_{2\mathrm{L}}} + \left(\frac{\partial\Delta\lambda_0}{\partial S_{2A}}\right)^2\sigma^2_{S_{2\mathrm{A}}} \\ &\simeq \left(\frac{\partial\Delta\lambda_0}{\partial R}\right)^2\sigma^2_{\mathrm{R}} + 2\left(\frac{\partial\Delta\lambda_0}{\partial S_2}\right)^2\sigma^2_{S_2} \\ &= \left[\frac{S_2}{(R+1)^2}\right]^2\sigma^2_{\mathrm{R}} + \left(\frac{R-1}{R+1}\right)^2\sigma^2_{S_2} \simeq \left[\frac{S_2}{(R+1)^2}\right]^2\sigma^2_{\mathrm{R}} \\ \sigma_{\Delta\lambda_0} &= \left[\frac{S_2}{(R+1)^2}\right]\sigma_{\mathrm{R}} \simeq \frac{S_2\sigma_{\mathrm{R}}}{4}. \end{aligned} \tag{A1}$$

In our calculations we have taken into account that, for the small Doppler shift that was measured in the TCABR, $R \simeq 1$ and the axial and lateral slits give approximately the same experimental uncertainty.

Equation (A1) shows that the uncertainty in the Doppler shift measurements is approximately equal to one-fourth of the uncertainty in the signal ratio measurements multiplied by the geometric image of the width of the exit slits. In our measurements of rotation velocity, the uncertainty in signal ratio was approximately equal to 2% for C III (4647.4 Å) and 5% for C VI (5290.6 Å); this means that the uncertainty in velocity is approximately 1 km s^{-1} for C III and 3 km s^{-1} for C VI. Figures 9 and 10 present experimental time series of the poloidal rotation velocity measured in a vertical chord

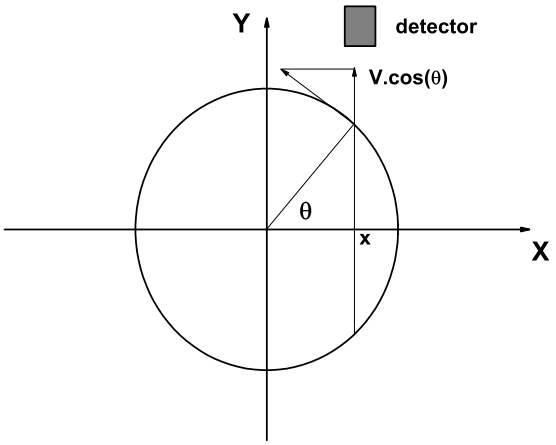

Figure 18. Schematic representation of the projection of vector velocity in the detector direction.

crossing the plasma centre. As can be seen in figures 9 and 10, the fluctuation of the experimental values around zero (the expected value) is consistent with the uncertainties estimated by (A1).

The time resolution, which in this experiment was 1 kHz, is connected to the velocity resolution; i.e. large time resolution implies smaller velocity resolution and vice versa. The reason for this is that with increased time resolution, the signal-to-noise ratio decreases and therefore the velocity resolution decreases.

More importantly, equation (A1) shows that the velocity resolution is found to be sensitive to the noise in signal ratio and improvement on velocity or time resolution can be obtained by reducing the noise in the photomultiplier signals.

Appendix B. The radial profile of the toroidal rotation velocity

To obtain the radial profile of plasma velocity we suppose that the plasma rotation velocity has the following profile $V(r) = c_0 + c_1 r + c_2 r^2 + c_3 r^3$, where c_0, c_1, c_2 and c_3 are parameters to be adjusted by a last-squares fit with experimental data.

The line-integrated energy flux detected by the detector installed at the lateral slit at wavelength $\lambda_L + \Delta\lambda_0 - \Delta\lambda_L/2$ to $\lambda_L + \Delta\lambda_0 + \Delta\lambda_L/2$ is equal to

$$\Phi_L = G_L b_E \int_x^{r_0} \int_{\lambda_L+\Delta\lambda_0-\frac{\Delta\lambda_L}{2}}^{\lambda_L+\Delta\lambda_0+\frac{\Delta\lambda_L}{2}} \frac{2r}{\sqrt{r^2-x^2}} \varepsilon(r) f(\lambda) \eta_L(\lambda) \mathrm{d}\lambda \, \mathrm{d}r, \tag{B1}$$

where G_L is a geometric factor that takes into account all geometrical dimensions of the optical system, b_E is the width of the entrance slit, $\varepsilon(r)$ is the emissivity, $f(\lambda)$ is the recorded function and $\eta(\lambda)$ is the coefficient of the transmission of the monochromator that for small wavelength interval $\Delta\lambda_L$ is assumed as constant in our case.

The integral of recorded function was calculated above and can be substituted in (B1), then

$$\Phi_L = G_L b_E \eta_L \frac{\Delta\lambda_L}{2 S_1 S_{2L}} \int_x^{r_0} \varepsilon(r)(S_{2L} + 2\cdot\Delta\lambda_0) \frac{2r\,\mathrm{d}r}{\sqrt{r^2-x^2}}. \tag{B2}$$

On the other hand, $\Delta\lambda_0$ can be rewritten as $\lambda_0 V \cos\theta / c$, where $V\cos\theta$ is the projection vector velocity in the detector direction (see figure 18), then

$$\Phi_L = G_L b_E \eta_L \frac{\Delta\lambda_L}{2 S_1 S_{2L}} \int_x^{r_0} \varepsilon(r) \left(S_{2L} + \frac{2\cdot\lambda_0 V(r) x}{rc} \right) \frac{2r\,\mathrm{d}r}{\sqrt{r^2-x^2}}, \tag{B3}$$

where V is the plasma velocity. For the axial slit we have

$$\Phi_A = G_A b_E \eta_A \frac{\Delta\lambda_A}{2 S_1 S_{2A}} \int_x^{r_0} \varepsilon(r) \left(S_{2A} - \frac{2\cdot\lambda_0 V(r) x}{rc} \right) \times \frac{2r\,\mathrm{d}r}{\sqrt{r^2-x^2}}. \tag{B4}$$

Taking the ratio

$$R = \frac{\Phi_L}{\Phi_A} = \frac{k_L \int_x^{r_0} \varepsilon(r) \left(S_{2L} + \frac{2\cdot\lambda_0 V(r) x}{rc} \right) \frac{2r\,\mathrm{d}r}{\sqrt{r^2-x^2}}}{k_A \int_x^{r_0} \varepsilon(r) \left(S_{2A} - \frac{2\cdot\lambda_0 V(r) x}{rc} \right) \frac{2r\,\mathrm{d}r}{\sqrt{r^2-x^2}}}, \tag{B5}$$

where $k_L = G_L b_E \eta_L \Delta\lambda_L / (2 S_1 S_{2L})$ and $k_A = G_A b_E \eta_A \Delta\lambda_A / (2 S_1 S_{2A})$. Let $k_L = k_A$ and $S_{2L} = S_{2A} \equiv S$, then R can be rewritten in the following way:

$$R = \frac{\int_x^{r_0} \varepsilon(r) \left(1 + \frac{2\cdot\lambda_0 V(r) x}{rcS} \right) \frac{2r\,\mathrm{d}r}{\sqrt{r^2-x^2}}}{\int_x^{r_0} \varepsilon(r) \left(1 - \frac{2\cdot\lambda_0 V(r) x}{rcS} \right) \frac{2r\,\mathrm{d}r}{\sqrt{r^2-x^2}}};$$

$$\frac{R-1}{R+1} = \frac{\frac{4\lambda_0 x}{cS} \int_x^{r_0} \varepsilon(r) V(r) \frac{\mathrm{d}r}{\sqrt{r^2-x^2}}}{\int_x^{r_0} \varepsilon(r) \frac{2r\,\mathrm{d}r}{\sqrt{r^2-x^2}}}. \tag{B6}$$

To solve the above integral equation we have represented the line emissivity profile by a bell-shaped function multiplied by exponential function as

$$\varepsilon(r) = \varepsilon_0 \left(1 - \frac{r^2}{r_0^2} \right) \exp\left(\alpha \frac{r^2}{r_0^2} \right),$$

where ε_0 and α are two adjustable parameters. As can be seen from (B6) the factor ε_0 is cancelled out which means that just the parameter α is necessary to compute the integral (B6). The use of this peaked function for emissivity can be justified if we compare the graphics of this function with the real profile of emissivity that has obtained in the T.F.R machine for different impurities [28]. Based on the viewing geometry, two line of sight emissivities were calculated related to parameter α as

$$\varepsilon(x=0) = 2\varepsilon_0 \int_x^{r_0} \left(1 - \frac{r^2}{r_0^2} \right) \exp\left(\alpha \frac{r^2}{r_0^2} \right) \mathrm{d}r,$$

and

$$\varepsilon(x=x_1) = 2\varepsilon_0 \int_x^{r_0} \left(1 - \frac{r^2}{r_0^2} \right) \exp\left(\alpha \frac{r^2}{r_0^2} \right) \frac{2r\,\mathrm{d}r}{\sqrt{r^2-x_1^2}}.$$

Expanding the exponential term in a Taylor series and taking the ratio we obtain a equation related to parameter α,

$$A\alpha^2 + B\alpha + C = 0, \tag{B7}$$

where

$$A=\frac{k_1 r_0^7}{2}\left(\frac{1}{5}-\frac{r_0^2}{7}\right)+\frac{1}{14r_0^6}\beta^7+\frac{1}{10r_0^4}\left(\frac{3x_1^2}{r_0^2}-1\right)\beta^5 +\frac{x_1^2}{r_0^4}\left(\frac{x_1^2}{2r_0^2}-\frac{1}{3}\right)\beta^3+\frac{x_1^4}{2r_0^4}\left(\frac{x_1^2}{r_0^2}-1\right)\beta,$$

$$B=k_1 r_0^5\left(\frac{1}{3}-\frac{r_0^2}{5}\right)+\frac{1}{5r_0^4}\beta^5+\frac{1}{3r_0^2}\left(\frac{2x_1^2}{r_0^2}-1\right)\beta^3 +\frac{x_1^2}{r_0^2}\left(\frac{x_1^2}{r_0^2}-1\right)\beta,$$

$$C=k_1 r_0\left(1-\frac{r_0^4}{3}\right)+\frac{1}{3r_0^2}\beta^3+\left(\frac{x_1^2}{r_0^2}-1\right)\beta,$$

where $k_1=\varepsilon(x_1)/\varepsilon(0)$ and $\beta=\sqrt{r_0^2-x_1^2}$. Substituting the parameter α in (B6) yields

$$\frac{R-1}{R+1}=\left[\frac{4\lambda_0 x}{cS}\int_x^{r_0}\left(1-\frac{r^2}{r_0^2}\right)\exp\left(\alpha\frac{r^2}{r_0^2}\right)\times[C_0+C_1 r+C_2 r^2+C_3 r^3]\frac{\mathrm{d}r}{\sqrt{r^2-x_1^2}}\right]\times\left[\int_x^{r_0}\left(1-\frac{r^2}{r_0^2}\right)\exp\left(\alpha\frac{r^2}{r_0^2}\right)\frac{2r\,\mathrm{d}r}{\sqrt{r^2-x_1^2}}\right]^{-1}. \quad \text{(B8)}$$

Solving the integral (B8) we obtain the following equation:

$$D\cdot C=b, \quad \text{(B9)}$$

where

$$C=\begin{pmatrix}c_0\\c_1\\c_2\\c_3\end{pmatrix},\qquad b=\begin{pmatrix}b_1\\b_2\\b_3\\b_4\end{pmatrix}\equiv(b_m),$$

where

$$b_m=\frac{cS}{4\lambda_0 x_m}\left(\frac{R_m-1}{R_m+1}\right)\left[-\frac{2\alpha}{5r_0^2}\beta^5+2\left(\frac{\alpha-1}{3r_0^2}-\frac{2\alpha x_m^2}{3r_0^4}\right)\beta^3 +2\left(\frac{x_m^2(\alpha-1)}{r_0^2}-\frac{\alpha x_m^4-r_0^4}{r_0^4}\right)\beta\right],$$

and $m=1$, 2, 3 and 4. The matrix D is equal to

$$\begin{pmatrix}d_{11}&d_{12}&d_{13}&d_{14}\\d_{21}&d_{22}&d_{23}&d_{24}\\d_{31}&d_{32}&d_{33}&d_{34}\\d_{41}&d_{42}&d_{43}&d_{44}\end{pmatrix}\equiv(d_{m,n}),$$

where $n=1$, 2, 3 and 4,
and

$$d_{m1}=\ln\left|\frac{r_0+\sqrt{r_0^2-x_m^2}}{x_m}\right|\left(\frac{x_m^2(\alpha-1)}{2r_0^2}-\frac{3\alpha x_m^4-8r_0^4}{8r_0^4}\right) +\left(\frac{\alpha-2}{4r_0}-\frac{3\alpha x_m^2}{8r_0^3}\right)\beta,$$

$$d_{m2}=-\frac{\alpha}{5r_0^4}\beta^5+\left(\frac{\alpha-1}{3r_0^2}-\frac{2\alpha x_m^2}{3r_0^4}\right)\beta^3 +\left(\frac{x_m^2(\alpha-1)}{r_0^2}-\frac{\alpha x_m^4-r_0^4}{r_0^4}\right)\beta,$$

$$d_{m3}=\ln\left|\frac{r_0+\sqrt{r_0^2-x_m^2}}{x_m}\right|\left(\frac{3x_m^4(\alpha-1)}{8r_0^2}-\frac{15\alpha x_m^6-24x_m^2 r_0^4}{48r_0^4}\right) +\left(\frac{r_0(\alpha+3)}{12}+\frac{3x_m^2(\alpha-1)}{8r_0}-\frac{5\alpha x_m^2(2r_0^2+3x_m^2)}{48r_0^3}\right)\beta,$$

$$d_{m4}=-\frac{\alpha}{7r_0^4}\beta^7+\left(\frac{\alpha-1}{5r_0^2}-\frac{3\alpha x_m^2}{5r_0^4}\right)\beta^5 +\left(\frac{2x_m^2(\alpha-1)}{3r_0^2}-\frac{3\alpha x_m^4-r_0^4}{3r_0^4}\right)\beta^3 +\left(\frac{x_m^4(\alpha-1)}{r_0^2}-\frac{x_m^2(\alpha x_m^4-r_0^4)}{r_0^4}\right)\beta$$

and R_m is the ratio of signals at radial position x_m.

The unknown coefficients can than be readily calculated by solving equation (B9). The result is shown in figure 17 together with the line-integrated measurements of toroidal plasma rotation, for poloidal positions of gas injection $\theta_*=0$ (outboard). The velocity inversion at the edge is clearly reproduced.

References

[1] Doyle E.J. *et al* 2007 Plasma confinement and transport *Nucl. Fusion* **47** S18–27 chapter 2
[2] Mikhailoviskii A.B. and Tsypin V.S. 1982 *Sov. Phys.—JETP* **56** 75
[3] Severo J.H.F. *et al* 2003 *Nucl. Fusion* **43** 1047
[4] Severo J.H.F. *et al* 2007 *Rev. Sci. Instrum.* **78** 043509
[5] Rozhansky V. and Tendler M. 1996 *Reviews of Plasma Physics* ed B.B. Kadomtsev (New York: Consultants Bureau) vol 19 p 147
[6] Bortolon A., Duval B.P., Pochelon A. and Scarabosio A. 2006 *Phys. Rev. Lett.* **97** 235003
[7] Reimerder H. *et al* 2007 *Phys. Rev. Lett.* **98** 055001
[8] Yoshida M. *et al* 2008 *Phys. Rev. Lett.* **100** 105002
[9] Scarabosio A., Bortolon A., Duval B.P., Karpushov A. and Pochelon A. 2006 *Plasma Phys. Control. Fusion* **48** 663
[10] Duval B.P. *et al* 2008 *Phys. Plasma* **15** 056113
[11] Rozhansky V. *et al* 2005 *J. Nucl. Mater.* **337–339** 291
[12] Pedrosa M.A. *et al* 2007 *Plasma Phys. Control. Fusion.* **49** B303
[13] Rautian S.G. 1958 *Sov. Phys.—Usp.* **66** 245
[14] Rosenbluth M.N. *et al* 1972 *Phys. Fluids* **15** 116
[15] Hazeltine R.D. 1974 *Phys. Fluids* **17** 961
[16] Claassen H.A. *et al* 2000 *Phys. Plasmas* **7** 3699
[17] Helander P., Fulop T. and Catto P.J. 2003 *Phys. Plasmas* **10** 4396
[18] Field A.R. *et al* 2003 *30th EPS Conf. on Controlled Fusion and Plasma Physics (St Petersburg, Russia, 2003)* presentation 3.165 http://epsppd.epfl.ch/StPetersburg/PDF/P2_148.PDF
[19] Nascimento I.C. *et al* 2005 *Nucl. Fusion* **45** 796
[20] Fussmann G., Meyer H. and Pasch E. 1996 *Contrib. Plasma Phys.* **36** 501
[21] Condrea I., Haddad E., Gregory B.C. and Abel G. 2000 *Phys. Plasmas* **7** 3641

[22] Bugaraya V.I. *et al* 1985 *Nucl. Fusion* **25** 1707
[23] Duval B.P., Joye B. and Marchal B. 1992 *Nucl. Fusion* **32** 1405
[24] Gohil P. *et al* 1992 *14th IEEE/NPSS Symp. on Fusion Engineering (San Diego, CA, 3 October 1991)* vols 1 and 2 pp 1199–204
[25] Burrell K.H. *et al* 2004 *Rev. Sci. Instrum.* **75** 3455
[26] Solomon W.M. *et al* 2008 *Rev. Sci. Instrum.* **79** 10F531-1
[27] Paul S.F. *et al* 2004 *Rev. Sci. Instrum.* **75** 4077
[28] Group T.F.R. 1978 *Plasma Phys.* **20** 207